Interface Components: Nanoparticles, Colloids, Emulsions, Surfactants, Proteins, Polymers

Bénard-Marangoni dendrites upon evaporation of a reactive ZnO nanofluid droplet: Effect of substrate chemistry

Patryk W#sik, Annela Seddon, Hua Wu, and Wuge H Briscoe

Langmuir, **Just Accepted Manuscript** • Publication Date (Web): 26 Mar 2019

Bénard-Marangoni dendrites upon evaporation of a reactive ZnO nanofluid droplet: Effect of substrate chemistry

Patryk Wąsik[a,b], Annela M. Seddon[a,c], Hua Wu[b], and Wuge H. Briscoe[b,]*

[a] Bristol Centre for Functional Nanomaterials (BCFN), HH Wills Physics Laboratory, University of Bristol, Tyndall Avenue, Bristol, BS8 1TL, UK

[b] School of Chemistry, University of Bristol, Cantock's Close, Bristol, BS8 1TS, UK

[c] School of Physics, HH Wills Physics Laboratory, Tyndall Avenue, University of Bristol, Bristol, BS8 1TL, UK

CORRESPONDING AUTHOR

* E-mail: wuge.briscoe@bristol.ac.uk; Phone: +44 (0)117 3318256

ABSTRACT

Evaporation of a particle laden sessile drop can lead to complex surface patterns with structural hierarchy. Most commonly the dispersed particles are *inert*. We have recently reported that, when the sessile drop contains *reactive* ZnO nanoparticles, solidified Bénard-Marangoni (BM) cells with dendritic micromorphology were formed in the residual surface pattern from *in situ* generated nanoclusters. Here we report the effect of substrate chemistry on the residual pattern from evaporation of nanofluids containing ZnO particles dispersed in a mixture of cyclohexane

and isobutylamine, by comparing three different substrates: glass, silicon and hydrophilized silicon. In particular, we performed a quantitative analysis of the BM cell size distribution and the cell morphological characteristics *via* the fractal dimension analysis. We find that the size dimension λ_{BM} of the dendritic Bénard-Marangoni cells varied on the different substrates, attributed to their different hydrophilicity and affinity for water molecules, evident from the different polar components γ^p in their surface free energy from the Owens-Wendt analysis. The average BM cell size was the smallest for the glass substrate (λ_{BM} = 289 μm), and comparable for the unmodified and UVO treated silicon wafers (with λ_{BM} = 466 μm and 423 μm, respectively). The fractal dimension analysis provided a quantitative description of the BM cells with complex structural hierarchy, highlighting the differences in the geometric features of the surface patterns resulting from different substrate chemistry. We also found that the fractal dimensions depended on the BM cell size, attributing it to two different regimes: the growing fractals and the maturing fractals.

KEYWORDS

Evaporation Induced Self-Assembly, nanoparticles, zinc oxide, dissolution, Bénard-Marangoni instabilities, coffee ring effect, fractal dimension analysis

INTRODUCTION

The Bénard convection, also known as the Bénard-Marangoni convection, was first observed by Henri Claude Bénard in 1900 as ordered hexagonal cells formed in a melted paraffin with graphite dusts (1-2). Intrigued by the observation, he performed comprehensive studies of such cellular vortices in a horizontal layer of different volatile liquids such as ethanol, diethyl ether, and benzene at room temperature, as well as non-volatile wax or spermaceti (whale oil), on a metallic plate heated to 50 – 100 °C (3-4). In 1916, Lord Rayleigh published first theoretical explanation of Bénard's results based on the stability analysis, which implicated buoyancy as

the driving force for the convective motion (5). However, it has been later shown, both experimentally (6) and theoretically (7), that the convective cells in Bénard's system were induced by variations in the surface tension caused by temperature fluctuations at the free fluid surface. Many studies on Bénard convections have since been reported (8).

Due to localized fluctuations in the droplet surface temperature, multiple Bénard cells can be induced, and dispersed solutes may form corrugated residual patterns of connected polygons templating the convective cells (9). This has been explored in the evaporation induced self-assembly (EISA) process (10-11) to produce various surface patterns. Some examples include porous films with a knotted-rope structure from zeolite silicalite nanoparticle suspensions dried on silicon (12), and honeycomb patterns from various suspensions, such as silver, cobalt, copper and barium ferrite nanocrystals dispersed in hexane or decane (13-14), polystyrene microspheres in aqueous solutions with added pentadecanoic acid (15-16), toluene solutions of poly(styrene-ran-butadiene) copolymer (17) or calcium carbonate particles (18), and polymethyl(methacrylate) dissolved in chloroform (19). In addition, the Bénard-Marangoni convection has also been employed to produce other types of structures, such as sol-gel derived titania (TiO_2) films using surface tension changing co-solvents (20), hexagonal and stripe-like patterns by varying substrate wettability (21), nanoporous TiO_2 films (22), and single-walled carbon nanotubes (23).

In these previous studies (1-2, 5-8, 10-19, 21), the dispersed particles were *inert*, and the residual pattern formation was governed by inter-particle forces and evaporation-induced solvent flows, which in turn could be influenced by particle size, concentration, solvent composition, or evaporation rate. We have recently shown (24-25) that rapid evaporation of a *reactive* ZnO nanofluid sessile drop can lead to the formation of hierarchical residual, and the mechanism was elucidated and described in some detail in Ref. (24) to account for the structural hierarchy on nano-/micro-/maco-scopic levels, combining video microscopy

observations of the capillary waves at the droplet surface and time-resolved transmission electron microscopy (TEM) and cryo-TEM observations of the constituent nanostructures inside the droplet at different stages of the evaporation process. Briefly, as a mixed solvent (chloroform/methanol/isobutylamine or cyclohexane/isobutylamine) droplet containing ZnO nanoparticles evaporates on a solid substrate, ZnO particles undergo rapid dissolution. The *in situ* generated molecular and particulate species collude with and modify the solvent flows in the evaporating droplet, which further self-assemble and self-organize into clusters. As the drop thins upon evaporation, Bénard-Marangoni (BM) instabilities are triggered, and the *in situ* self-assembled clusters track the BM convections. Such BM convections manifest as multiple vortices with liquid flowing upward in the center and subsequently outward to the edge of the convection cells. Further removal of solvent upon evaporation leads to solidification and crystallization of the polycrystalline cellular pattern in the drop center with dendritic micromorphology.

The initial moisture-assisted dissolution of isobutylamine-coated ZnO nanoparticles was recognized as a key step in this process. We have shown that different crystallinity of the ZnO nanoparticles led to different dissolution rates, which in turn resulted in different surface patterns (26). These results may open up new routes for facile fabrication of functional surface patterns with hierarchical structures *via* self-assembly induced by evaporation of *reactive* nanofluids.

The solvent flow in an evaporating droplet is affected by several other factors, which will consequently affect the BM convection and the residual pattern. In this work, we have investigated how the substrate surface chemistry would affect the morphology of the surface patterns produced. Three different substrates, *i.e.* a glass coverslip, a silicon wafer, and a UVO treated silicon wafer, were compared. Their surface chemistry was assessed with the static contact angle (CA) measurement and their roughness by atomic force microscopy (AFM). In

addition, three types of ZnO particles with different sizes and crystallinities (26) were dispersed in a mixture of cyclohexane and isobutylamine, which were used to form the evaporating sessile drops. The resulted hierarchical surface patterns were analyzed by scanning electron microscopy (SEM). We found that the dimensions of the solidified Bénard cells depended on the substrate used due to different BM flows on these substrates. To go beyond a descriptive account of the surface pattern, the quasi-2D BM convection cells were analyzed using the box counting fractal dimension (FD) analysis (27) that provided a quantitative description of the BM cells with complex structural hierarchy, highlighting the differences in the geometric features of the surface patterns resulting from different substrate chemistry. We show that the surface chemistry of the substrate influences the dimension of the solidified BM cells during the ZnO nano/microfluid evaporation, and we discuss this effect in terms of the substrate-water interactions, as water is crucial to the ZnO nanocrystal dissolution in the pattern formation mechanism from such reactive nanofluids.

MATERIALS AND METHODS

ZnO nano/microparticles

Three different types of zinc oxide (ZnO) particles were used: in-house synthesized ZnO nanoparticles, and commercially acquired ZnO nanopowder (Sigma-Aldrich, <100 nm particle size, ~80% Zn basis), and ZnO powder (Sigma-Aldrich, ACS reagent, ≥99.0% (KT)). The in-house ZnO nanoparticles were synthesized using a modified procedure from Sun *et al*. (28). Transmission electron micrographs of the ZnO particles can be found in Supplementary Information, SI.01, also shown as insets in Figure 5. Detailed characterization of ZnO particles including transmission electron microscopy, particle size distribution, X-ray diffraction, and energy-dispersive X-ray spectroscopy as well as synthesis of the in-house ZnO nanoparticles is reported elsewhere (26).

ZnO nano/microfluid preparation

ZnO nano/microfluids were prepared by dispersing ZnO particles in a mixture of cyclohexane (Fisher Chemicals, assay 99%) and isobutylamine (Sigma-Aldrich, assay 99%), in a 5:1 volume ratio to 1 mg/mL concentration. As prepared suspensions were sonicated for 2 h to form homogeneous dispersions prior to evaporation experiments. Dynamic light scattering data of ZnO nano/microfluid has been reported in (26), which indicated formation of clusters (1 - 2 μm in size) in all ZnO nano/microfluids, as the suspensions were not inherently stable.

Substrates

Evaporation of the ZnO nano/microfluids sessile drops were performed on three different substrates cut into 1×1 cm^2 squares, including standard microscope glass slides (type 7101, 0.8 - 1.0 mm thick), and silicon wafers (UniversityWafer Inc., ID 452, 100 mm diameter, P type, B dopant, <100>, 0-100 Ω·cm, 500 μm thick, single-sided polish, test grade), either unmodified or treated by UV/ozone (UVO) exposure for 10 min. The substrates were cleaned by sonication in acetone and ethanol sequentially for 10 min each, rinsed three times with *Milli-Q* water (18.2 MΩ·cm at 25 °C), then sonicated in *Milli-Q* water for 10 min and dried using a stream of nitrogen prior to the experiment. For the UVO treatment, a 42-220 UVO-Cleaner (Jetlight Company, Inc.) was used to modify the surface chemistry of the Si substrates, making them more hydrophilic by increasing the amount of -OH groups on the surface (29-30) (see SI.02). Both the contact angle measurements and evaporation experiments were performed within 1-2 h of the UVO treatment.

The wettability of the substrates was characterized using sessile droplet static contact angle measurements of probing liquids such as Milli-Q water (18.2 MΩ·cm at 25 °C), diiodomethane (Alfa Aesar, 99%), ethylene glycol (Fluka Analytical, ≥ 99.5%), n-hexadecane (Acros Organics, 99%, pure), n-dodecane (Acros Organics, 99%, pure), cyclohexane (Fisher Chemicals, assay 99%), and a mixture of cyclohexane and isobutylamine (Sigma-Aldrich,

assay 99%) in a 5:1 volume ratio, in addition to ZnO nano/microfluids prepared from the in-house synthesized ZnO nanoparticles and commercially acquired ZnO nanopowder and ZnO powder (see SI.01) dispersed in the mixture of cyclohexane and isobutylamine 5:1 volume ratio to 1 mg/mL concentration (see the main text). The measurements were performed at room temperature of 24.5 ± 0.5 °C and relative humidity of ~45% (monitored with a humidity/temperature pen (Tracable)) using a Drop Shape Analyzer – DSA100 (KRÜSS) operated with the KRÜSS ADVANCE 1.9.0.8 software. In a typical measurement, a 5 μL droplet of the measurement liquid (30 μL for cyclohexane/isobutylamine mixture) was pipetted onto a 1×1 cm^2 substrate, and the image of the drop was recorded for 60 seconds in one second intervals. The value of the contact angle was obtained by tangent fitting method to the drop shape using the software. The errors in mean CA values are quoted as the standard deviations from: 20, 37, and 26 separate measurements for the in-house ZnO nanofluid on glass, unmodified Si, and UVO exposed Si, respectively; 12, 62, and 35 for ZnO nanopowder nano/microfluid on glass, unmodified Si, and UVO exposed Si, respectively; and 8, 25, and 6 for ZnO powder nano/microfluid on glass, unmodified Si, and UVO exposed Si, respectively. Surface free energies were calculated according to the Owens-Wendt method (31), based on the sessile droplet CA measurements of *Milli-Q* water and diiodomethane (see SI.03). Substrate topography was characterized with the atomic force microscopy (AFM) using MultiMode Nanoscope III (Bruker) operated in the tapping mode (see SI.04)

Evaporation of reactive ZnO nanofluid droplets

An air displacement pipet was used to drop-cast 30 μL of ZnO nano/microfluids onto the surface of the substrates, which were placed inside compartments of an uncovered polystyrene Petri dish (Sterilin, 25 compartment sterile 100 mm box). The evaporation took place at room temperature and RH ~45%. The substrates were covered with white deposits within several

minutes of evaporation. In the case of UVO-Si, the evaporation experiments were performed within 1-2 h after the UVO treatment.

Residual surface pattern characterization

Residual surface patterns formed from ZnO nano/microfluids were analyzed with scanning electron microscopy (SEM) using a JSM-IT300 SEM, JEOL. Microfocus grazing incidence X-ray diffraction (XRD) characterization has confirmed (26) that the residual surface patterns produced from the in-house ZnO nanofluid were composed almost entirely from layered complexes of zinc hydroxide with anionic interlayer species (interplanar spacing of 1.37 nm and 0.68 nm, indexed as (001) and (002) planes), and brucite-type zinc hydroxide (interplanar spacing of 0.27 nm and 0.52 nm, indexed as (100) and (110) planes) structures. There were also partial contributions (~5% of diffraction signal) of a ZnO phase. For the residual patterns produced from the commercially sources ZnO particles, the diffraction profiles were dominated by ZnO patterns from undissolved ZnO nano/microcrystals forming aggregates that were deposited across the fibrous network of the residual patterns.

Bénard-Marangoni (BM) cells size distribution analysis

Size distribution analysis of the BM cells was performed using ImageJ (version 1.51j8) software. First, the individual BM cells were outlined on their SEM images using the Serif DrawPlus X6 software, then manually separated to eliminate overlaps for analysis. The size distribution of the BM cells was fitted with the lognormal distribution function (see SI.06).

Fractal dimension analysis

The complex structural hierarchy of BM cells was analyzed using the box counting fractal dimension (FD) analysis, as described in detail in (27). Briefly, in the box counting algorithm, a grid of equal boxes of a side-length ε is laid over an image, and then the number of non-empty boxes, $N(\varepsilon)$, is counted. This number varies with the box size, $N(\varepsilon) \sim \varepsilon^{-D}$, and the

procedure is performed for a range of ε values. The box counting fractal dimension, D, is obtained from the slope of the ln(N) *vs*. ln(ε) plot (32-33). Specifically for the analysis of the BM cells, the SEM images of the pattern were converted to the binary format in ImageJ, and then circular selections containing BM cells were analyzed using FracLac (version 2015Sep090313a9330) plugin (34). The analysis process is schematically displayed in **Figure S12**. For completeness, we also include in SI.07 a description of the analysis, which is also described in the SI section of Ref. (27).

RESULTS AND DISCUSSION

Substrate characterization: Surface energy and roughness

The surface energy of the three different substrates, microscope glass slide, silicon wafer and UVO hydrophilized silicon (UVO-Si) wafer, was assessed with the static contact angle (CA) measurement using different solvents (see SI.03 for details). The results are presented in **Table 1**. The mean CA values measured with a 5 μL droplet of three ZnO nano/microfluids were similar across the substrates, *ca.* $\theta \approx$ 5.5 - 6.5°, with the in-house ZnO nanofluid showing a slightly higher CA on glass ($\theta = 8.6 \pm 2.0°$) and ZnO powder nano/microfluid a slightly lower CA on UVO-Si ($\theta = 4.1 \pm 1.9°$).

The mean *water* CA was $\theta = 21.7 \pm 3.5°$ on the microscope glass slide, $\theta = 56.5 \pm 1.2°$ on the silicon wafer, and $\theta = 9.8 \pm 1.6°$ on UVO-Si. These broadly agree with the literature values, *i.e.* $\theta \sim 31°$ for glass, $\theta \sim 58°$ for silicon with native SiO_2 (35), and $\theta \sim 10°$ for UVO exposed silicon, respectively (36). Thus, all the substrates exhibited a certain degree of hydrophilicity, with the UVO-Si most hydrophilic, and untreated Si least.

For the evaporation experiment, the 30 μL droplets would become pinned at the edge with an apparent pinned CA of $\theta \sim 26$ - 27° on all the substrates. This is comparable to the pinned CA of the control droplets of cyclohexane/isobutylamine mixtures on the substrates ($\theta \sim 26$ -

27°) also shown in **Table 1**. The pinned CA values are higher than those for the static CA. As the evaporation took place, the pinned droplet would thin, and the apparent CA at the pinned periphery would decrease to the values of respective nano/microfluids, before the contact line receded upon further evaporation.

The calculated surface free energies (SFE) of the substrates based on the Owens-Wendt method (31) using droplets of *Milli-Q* water and diiodomethane (see SI.03 for details) were γ = 74.4 ± 1.5, 50.3 ± 1.6, and 75.5 ± 0.5 mN/m for the microscope glass slide, Si, and UVO-Si, respectively. The UVO-Si had the largest polar SFE contribution (γ^P = 36.4 ± 0.3 mN/m), consistent with its smallest water CA. The unmodified Si had the lowest values of disperse and polar components in the surface energy, γ^D = 33.1 ± 0.8 and γ^P = 17.2 ± 0.8 mN/m, respectively. We note that slightly different surface energy values of diiodomethane exist in the literature, *e.g.* γ^D = 48.5 (or 49.5) mN/m and γ^P = 2.3 (or 1.3) mN/m in Ref. (37). The values of γ^D = 50.8 mN/m and γ^P = 0 mN/m have been used in this study as in Refs. (38-40). Resolving this small controversy is beyond the scope of this study. However, the small differences in the surface energy values (cf. **Table S6**) do not affect the discussions presented here, as discussed in SI.03.

In addition, the topography of the substrate surface was characterized with AFM imaging (see SI.04). The surface roughness expressed in both R_a (arithmetic average roughness) and R_{rms} (root mean square average roughness) parameters (**Table S7**) increased slightly in the order from glass (R_a = 0.09 nm, R_{rms} = 0.11 nm), to unmodified silicon (R_a = 0.14 nm, R_{rms} = 0.17 nm), and UVO treated silicon (R_a = 0.17 nm, R_{rms} = 0.22 nm). All the substrates were however all relatively smooth, manifesting in a very low (< 0.2 nm) arithmetic average roughness, R_a.

Table 1. Surface free energies (SFEs) and wettability of the substrates. The mean contact angle (CA) measurements between different substrates and droplets (5 μL) of *Milli-Q* water,

diiodomethane, ZnO nano/microfluids (in cyclohexane/isobutylamine 5:1 mixtures), and pinned CA of the control mixture (30 μL droplet, pinned CA). The SFEs were calculated using the Owens-Wendt method (31) (see SI.03, in which we note other methods also exist (*e.g.* Neumann, Fowkes, Owens-Wendt-Rabel-Kaelble, van Oss-Chaudhury-Good, and Zisman).

	Microscope glass slide	Silicon wafer (Si)	UVO silicon wafer (UVO-Si)
Testing fluids	Mean contact angle (CA) θ		
In-house ZnO nanofluid	8.6 ± 2.0°	5.7 ± 1.2°	6.5 ± 1.7°
ZnO nanopowder nano/microfluid	5.5 ± 1.0°	6.0 ± 1.9°	5.5 ± 2.0°
ZnO powder nano/microfluid	5.6 ± 1.1°	5.9 ± 1.8°	4.1 ± 1.9°
Milli-Q water	21.7 ± 3.5°	56.5 ± 1.2°	9.8 ± 1.6°
Diiodomethane	29.6 ± 0.5°	52.0 ± 1.3°	41.1 ± 0.9°
Cyclohexane/isobutylamine mixture (pinned)	29.4 ± 4.3°	26.7 ± 1.5°	27.2 ± 2.4°
	Surface free energy (mN/m)		
Total γ	74.4 ± 1.5	50.3 ± 1.6	75.5 ± 0.5
Dispersive component γ^D	44.4 ± 0.2	33.1 ± 0.8	39.0 ± 0.2
Polar component γ^P	30.0 ± 1.3	17.2 + 0.8	36.4 ± 0.3

Descriptive account of the BM cells on three different substrates from ZnO nanofluid sessile drops

An example of the residual surface pattern formed from the in-house synthesized ZnO nanoparticle (diameter ~ 9 nm) dispersion on hydrophilized UVO-Si is shown in **Figure 1**. (Figure 1a, d, and f are adapted from Ref. (27), which focused on the fractal dimension analysis. These results are included here to compare with the results on two other substrates shown in Figure 2 and Figure 3 below, for clarity and completeness.) It was composed of a central region with packed cellular structures surrounded by a coffee ring around the perimeter of the droplet

(**Figure 1b-c**), comprising a dense network of intercalating fibers (**Figure 1c**). The central region of the residual surface pattern consisted of circular patches or cells – identified as solidified Bénard-Marangoni (BM) convection cells, with their diameters corresponding to the BM wavelength (λ_{BM} = 200 - 800 μm). The micromorphology of the cells resembles spoke-like patterns with a bow-tie projection (**Figure 1d**). Their appearance was also similar to the BM flow pattern observed during the evaporation of toluene from polystyrene/toluene solution [14]. One of the well-defined cells is shown in **Figure 1f** (whose fractal dimension analysis has been shown in detail in (27). The Marangoni number, B, which gauges the balance between the surface tension and the viscous force in a fluid, depends on the parameters such as the temperature gradient across the drop thickness, and the thermal diffusivity, dynamic viscosity, thermal conductivity, density, and specific heat capacity in the drop (7). For the fluid conditions with $B > 80$, spontaneously generated surface-tension driven flows will result in the formation of BM cells. For a drop of thickness d, the ultimate BM cell size or wavelength, λ_{BM}, is related to the Marangoni number by:

$$B = 32\left(\frac{\pi d}{\lambda_{BM}}\right)^2. \quad (1)$$

Wu and Briscoe (24) estimated that, in their ZnO nanofluid (ZnO nanoparticles dispersed in a mixture of chloroform, methanol and isobutylamine), the Marangoni number was much larger ($B \sim 300$ - 2000) than the critical value of 80 (24). They attributed the formation of the BM cells to the fluctuations in the fluid viscosity due to the variation in the local particle concentration during evaporation. It was also shown (24) that slow evaporation would not lead to the BM cell formation, which could be attributed to the insufficient temperature gradient across the thickness of the drop required to initiated the BM flow. Here we have observed λ_{BM} = 200 - 800 μm, giving a critical thickness range d = 100 – 400 μm at which the BM instabilities were triggered. This variability is consistent with the interpretation that the concentration of the *in situ* generated molecular clusters and particulate species in the reactive ZnO nanofluid

was inhomogeneous inside the drop, leading to BM being triggered at different evaporation stages.

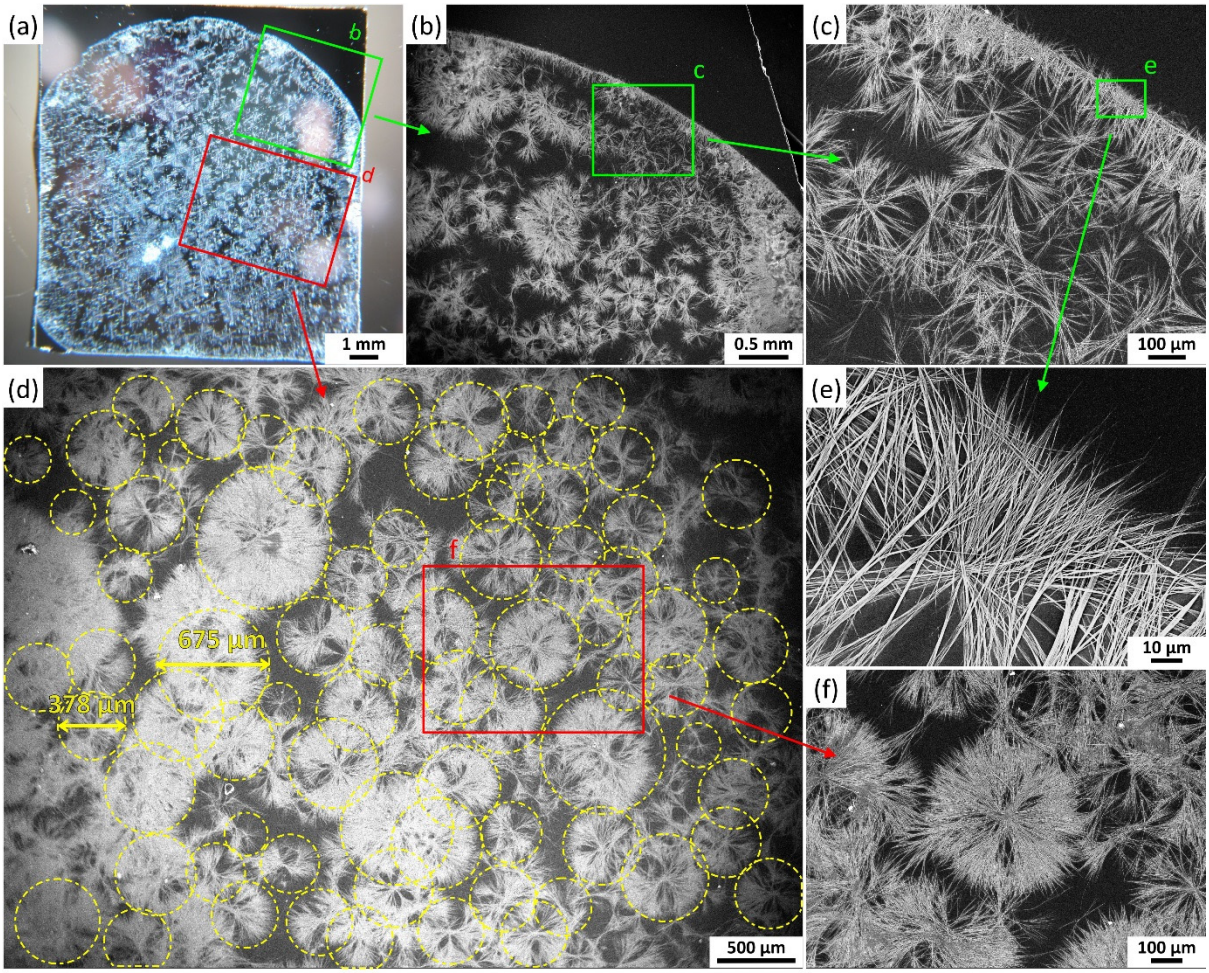

Figure 1. Residual surface pattern formed from a 30 µL sessile drop of the in-house synthesized ZnO nanofluid droplet dried on the UVO treated silicon wafer (UVO-Si): (a) overall optical microscopy image of the pattern; (b-c) enlarged views of an SEM image of a section close to the peripheral coffee ring; (d) a magnified view of a SEM image of the central region that reveals spoke-like patterns with a bow-tie projection, identified as solidified manifestation of Bénard-Marangoni (BM) convection cells; (e) intercalated fibers in the coffee-ring edge; and (f) a magnified view of a BM convective cell. Images in (a), (d), and (f) are adapted from Ref. (27) *J. Colloid Interface Sci.*, 2019, 536, Patryk Wąsik, Annela M. Seddon, Hua Wu, Wuge H. Briscoe, Dendritic surface patterns from Bénard-Marangoni instabilities upon evaporation of

a reactive ZnO nanofluid droplet: A fractal dimension analysis, 493-498, Copyright (2019), with permission from Elsevier.

Figure 2 shows that, similar to the residual pattern on UVO-Si, the glass surface was covered with solidified BM convection cells with overall smaller diameters, λ_{BM} = 200 - 500 µm (**Figure 2b-c**). The packing density of the fibers inside BM cells appeared smaller, leading to a higher degree of interpenetration between different BM cells. **Figure 2d** shows the fibers constituting the BM cells, which are re-crystallized from gel-like fibers self-assembled from *in situ* generated clusters, as discussed in detail in Ref (24).

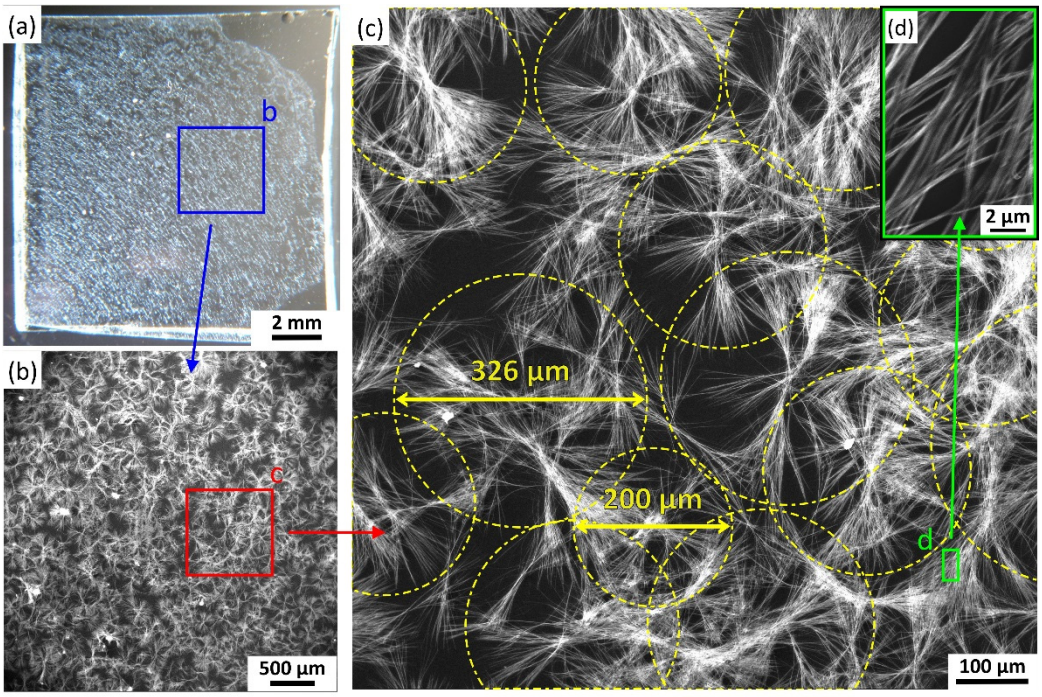

Figure 2. Residual surface pattern formed from a 30 µL sessile drop of the in-house synthesized ZnO nanofluid droplet dried on a microscope glass slip: (**a**) overall optical microscopy image; (**b**) an SEM image of a section in the central region; (**c**) an enlarged view of the central region from (c) showing solidified manifestation of Bénard-Marangoni (BM) convection cells marked by yellow dotted circles; and (**d**) an enlarged view showing the fibrous structure constituting the BM cell.

An example residual surface pattern from the in-house synthesized ZnO nanofluid on an unmodified silicon wafer is presented in **Figure 3**. Similar to the other two substrates, the central region of the substrate was covered with solidified BM cells with a wide range of diameters, *i.e.* λ_{BM} = 250 - 1000 μm, with the fiber-packing denser than those on the glass slide (*cf.* **Figure 2**) and also with significant interpenetrations at the BM cell peripheries.

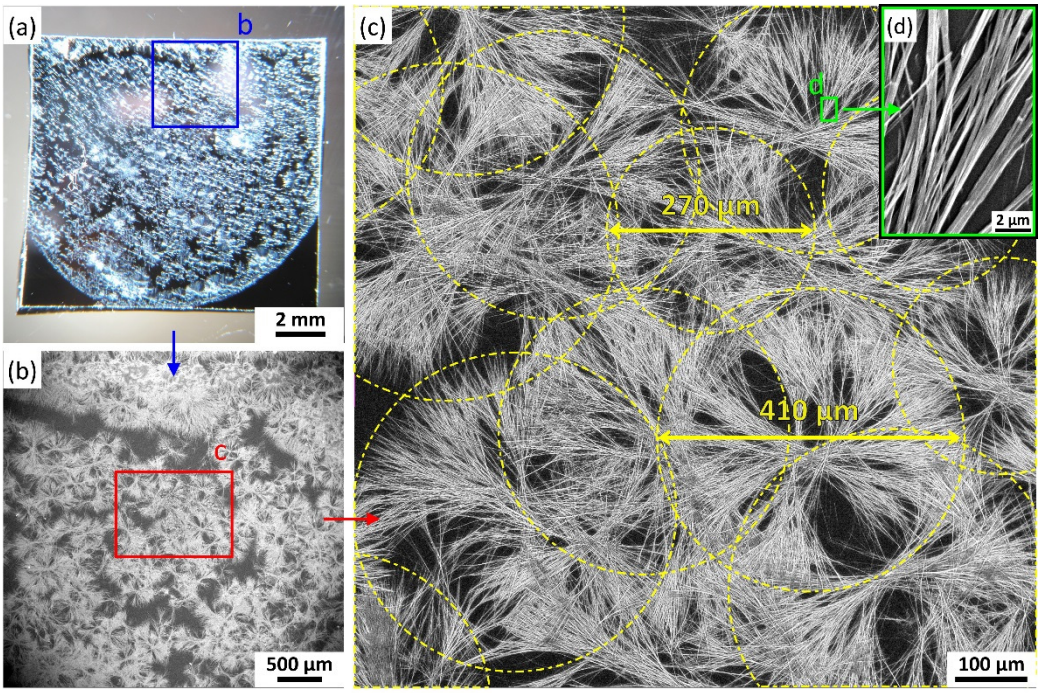

Figure 3. Residual surface pattern formed from a 30 μL sessile drop of the in-house synthesized ZnO nanofluid droplet dried on an unmodified silicon wafer (Si): (**a**) overall optical microscopy image; (**b**) an SEM image of a section in the central region; (**c**) an enlarged view of the central region in (c) showing solidified Bénard-Marangoni (BM) convection cells with borders marked by yellow dotted circles; and (**d**) an enlarged view showing the fibrous structure constituting the BM cell.

Bénard-Marangoni (BM) cell size λ_{BM} distributions on three different substrates

The size distributions of the BM cells in the central region of the residual surface patterns were fitted with the log-normal distribution function (SI.06), with *M* denoting the geometric mean of the BM cell size λ_{BM} (*i.e.* the median size) by count and σ_g its geometric standard

deviation (*i.e.* the skewness and dispersion of the size distribution) (41). 68.3% of all the BM cells had the size between M/σ_g and $M \cdot \sigma_g$ (42).

The solidified BM cells showed different size distributions on the three different substrates (*i.e.* glass, silicon and UVO exposed silicon), and the results from the in-house synthesized ZnO nanofluid (~ 9 nm nanoparticle diameter) are presented in **Figure 4**. The smallest mean diameters (M = 289 μm, **Figure 4a**) were observed on the glass substrate, with the smallest polydispersity (σ_g = 1.25, *i.e.* 68.3% of λ_{BM} values lying in the range 252-375 μm). The BM cells on Si (**Figure 4b**) showed the largest mean sizes (M = 466 μm), with a slightly higher diameter dispersion (σ_g = 1.27; 68.3% of λ_{BM} in the range 367-592 μm). By comparison, λ_{BM} on UVO-Si (**Figure 4c**) showed slightly smaller mean size values (M = 423 μm), with the highest dispersion parameter σ_g = 1.30 (*i.e.* 68.3% of λ_{BM} in the range 325-550 μm.

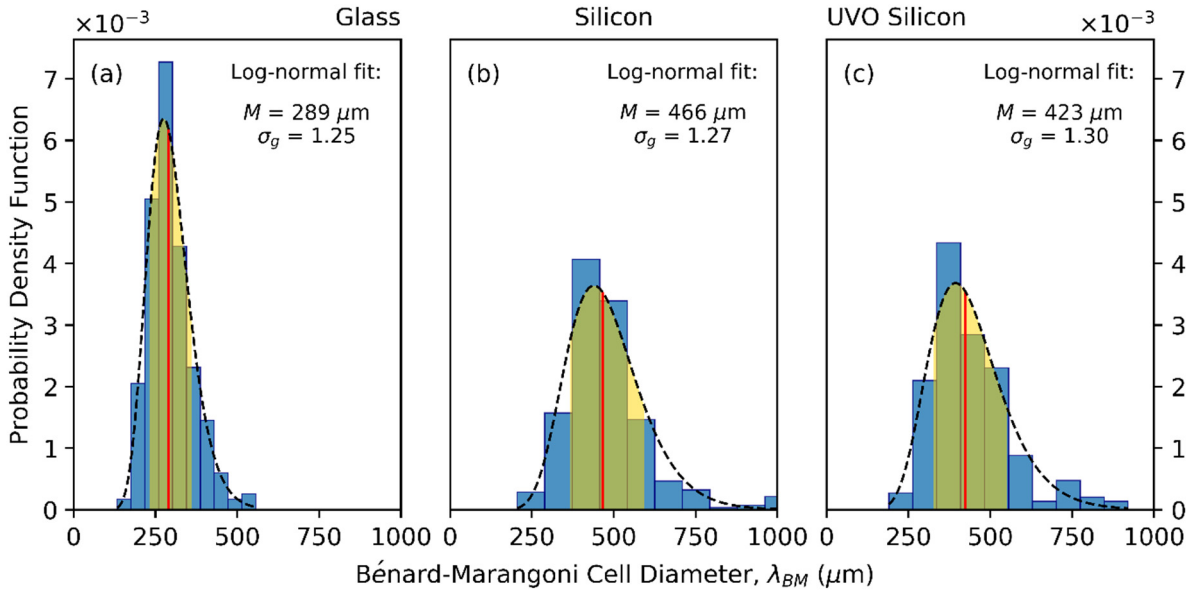

Figure 4. Size distributions of λ_{BM} as the probability density function (PDF) of the BM cells in the central region of the residual surface patterns from the in-house synthesized ZnO nanofluid on the three different substrates: (**a**) microscope glass slide, (**b**) Si, and (**c**) UVO-Si. BM cell sizes distributions were fitted with the log-normal distribution function (dashed lines) (SI.06). Red vertical lines indicate the geometric mean M. BM cell sizes between M/σ_g and

$M \cdot \sigma_g$ (68.3% of all values) are shaded in the golden-yellow color under the size distribution curves.

Residual patterns were also studied using the commercially acquired ZnO nanopowder and ZnO powder (*cf.* **Figure S1** in SI.01; at the same particle concentration of 1 mg/mL in the same solvent mixture, cyclohexane and isobutylamine in 5:1 volume ratio), which exhibited a wide range of sizes and morphologies. **Figure S8** shows the SEM images of the central regions of the residual surface patterns from ZnO nanopowder and ZnO powder nano/microfluid droplets on glass, Si, and UVO-Si. The central regions of these patterns were also composed of solidified BM cells, with the dendritic fibers radiating from the cell center. In contrast to the results obtained for the in-house synthesized ZnO nanofluid (**Figure 1** - **Figure 3**), the overall surface coverage and the fiber density in the BM cells were much higher, and there was also more significant inter-cell penetration. The optical microscopy of the overall patterns with the droplet footprints are shown in **Figure S9** and **Table S6**.

A trend in the BM cell size distribution with respect to the substrate was similar to that observed with the in-house ZnO nanofluid. Specifically, the geometric mean BM cell size, *M,* and the geometric standard deviation coefficient, σ_g, increased in the order of glass, unmodified silicon and UVO treated silicon, confirming that the BM cell size depended on the substrate (**Figure 5**). The smallest *M* value was observed for the commercially acquired ZnO powder dried on glass (M = 106 μm), and the biggest BM cells were created from the commercially acquired ZnO nanopowder on UVO-Si (M = 515 μm).

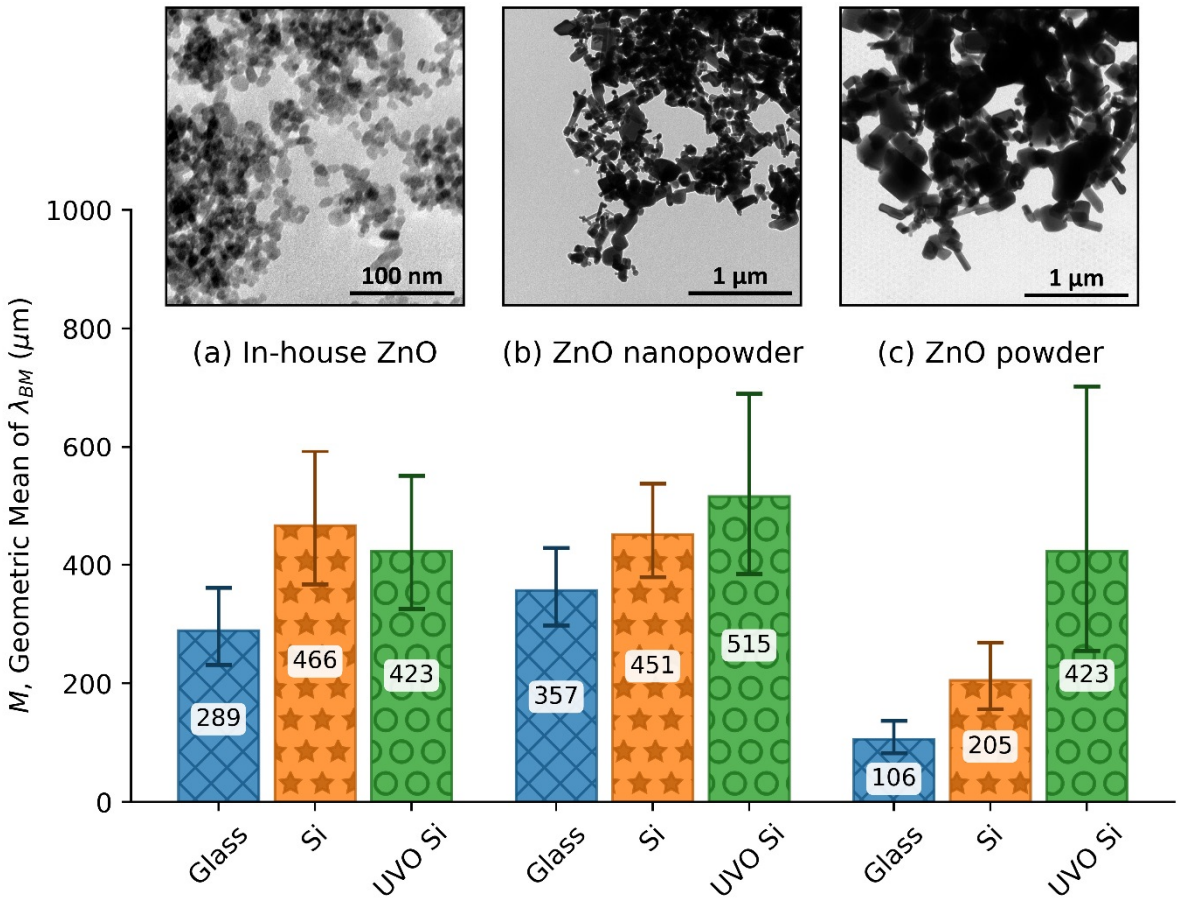

Figure 5. Geometric mean size M of Bénard-Marangoni cell size λ_{BM} distribution produced from different nano/microfluids: (**a**) the in-house synthesized ZnO, (**b**) ZnO nanopowder, and (**c**) ZnO powder; formed on different substrates: glass (blue bars with cross "X" pattern), Si (orange bars with star "★" pattern), and UVO-Si (green bars with circle "O" pattern). The corresponding TEM images of the ZnO particles in the droplet dispersions are shown at the top. The error bars are calculated as M/σ_g and $M\cdot\sigma_g$ for lower and upper errors, respectively, showing the distribution of λ_{BM}.

Box counting fractal dimension (FD) analysis of Bénard-Marangoni (BM) cell micromorphology

The results of the box counting fractal dimension (FD) analysis of the solidified BM cells on different substrates are presented in **Figure 6**, and all the FD values were in the range $D \approx 1.66$

- 1.89. The fractal dimension of a pattern reflects its geometrical properties, *i.e.* how much space it fills when it is scaled up or down or the prominence of its irregularities (43). It can also be used to quantify the ruggedness of particle boundaries (44). Fractal dimensions, in contrast to topological dimensions, can take non-integer values. For reference, a line is 1-dimentional, a surface is 2-dimensional, and a cube is 3-dimensional object. Classical fractals such as the Koch snowflake or the Sierpiński triangle have dimensions of $D \approx 1.262$ and 1.585, respectively (45). If these structures are scaled up, the Sierpiński triangle would cover more area than the Koch snowflake. However, both of them would cover less area than a scaled up square ($D = 2$), which would fill the entire area; but more than a scaled line ($D = 1$), which would not fill any area at all (43). The distribution of the D values for the BM cells was calculated as a probability density function (PDF) as shown in **Figure 6a**, **c** and **d** (left hand side). The fitting parameters, μ and σ, the mean value and its standard deviation respectively, are also listed in the figure for the normal distribution fits, shown as dashed lines h_1, h_2 and h_3, respectively for glass, Si and UVO-Si and for different ZnO nano/microfluids. In addition, the apparent trends in the mean value and its standard deviation of fractal dimension distribution are shown in **Figure 7**.

The BM cells formed from the in-house ZnO nanofluid on the glass substrate (h_1 in **Figure 6a**) had the lowest average D value of $\mu = 1.77$ with the highest dispersion of $\sigma = 0.04$, amongst all samples (**Figure 7**). BM cells formed on both unmodified and UVO treated silicon resulted in higher and less dispersed D values, with $\mu = 1.84$ ($\sigma = 0.02$) and 1.82 ($\sigma = 0.03$), respectively (h_2 and h_3 in **Figure 6a**). The scatter in the D values is qualitatively consistent with our interpretation that there were local inhomogeneities in the viscosity and thermal properties in a drying droplet. The various flow rates and solute concentrations involved in the self-assembly process in different BM flow cells would result in a different packing in the dried cell, and in turn different fractal dimension values.

The D values for the BM cells from the other ZnO particles exhibited a smaller scatter (D ~ 1.82 – 1.84). For the ZnO nanopowder BM cells, these values were, μ = 1.83 (σ = 0.01), 1.83 (σ = 0.03), and 1.84 (σ = 0.02), on glass, Si, and UVO-Si (h_1, h_2, and h_3 in **Figure 6c**, and **Figure 7c**), respectively. Similarly for the BM cells produced from the ZnO powder nano/microfluid, the corresponding values are μ = 1.82 ($\sigma \approx$ 0.02), 1.84 (σ = 0.03), and 1.84 (σ = 0.02), on the three substrates (h_1, h_2, and h_3 in **Figure 6e**, and **Figure 7b**).

Variation of BM cell fractal dimension with its size: Growing fractals vs. maturing fractals

The fractal dimension values are also plotted against BM cell diameters (D *vs*. λ_{BM}) on the right hand side of **Figure 6** (**b**, **d** and **f**). There appears a general trend that D increases with λ_{BM} for all the conditions investigated, a trend that has also been observed from a benchmark FD analysis of classic fractals such as a hexaflake and the Sierpiński carpet (27) (also see SI.07). The rate of increase is much higher for small BM cell diameters of $\lambda_{BM} < 200$ μm, before a plateau is reached for higher λ_{BM} values. The data for different substrates is enveloped in colored areas for comparison. This trend is consistent with the observation that the BM cells had a more open structure (and thus smaller surface coverage) towards the cell centre, leading to smaller D values for smaller λ_{BM}. As a result, the BM cells with bigger diameters exhibited larger D values, and thus had more rugged structures. This is an interesting result. A fractal is characterized by its constant FD value as it is scaled up or down. Here we show that the solidified BM cells and the classical fractal patterns all display a smaller D value for smaller fractals, and their fractal dimensions then reached a plateau value that is consistent to what has been reported in the literature. We suggest that the FD analysis has revealed two regimes of the fractal growth: an initial stage of growing fractals with a more open structure and a subsequent stage of maturing fractals, and this trend has not been reported previously.

The trend may be fitted to a logarithmic function, $y = a \ln(\lambda_{BM}) + D_0$, shown as the dashed lines in the figure labelled as y_1, y_2 and y_3 for the patterns on glass, Si, and UVO-Si, respectively (**Figure 6b**, **d** and **f**). It should be acknowledged that the choice of the function is arbitrary, mostly as a guide for the eye. We discuss the physical meanings of the fitting parameters in a qualitative manner to compare different conditions. A different fitting function would have equally described the trend (*e.g.* a polynomial), but the discussion below is qualitatively valid and internally consistent.

A smaller D_0 and larger a can be indicative of the presence of more voids (*i.e.* unoccupied areas) towards the center of the dendritic pattern of a BM cell. The BM cells from the ZnO powder resulted in the highest intercept values D_0 (in the range of 1.71 - 1.80), and the lowest a values in the range of 0.01 - 0.02, for all the investigated substrates, indicating the highest fibre density in the BM cells. This is followed by patterns from the ZnO nanopowder on glass and UVO-Si, with D_0 values equal to 1.69 and 1.71, and a values ~ 0.03 and 0.02, respectively. However, the results from the patterns produced from the ZnO nanopowder nano/microfluid on Si (D_0 = 1.51, a = 0.06) are similar to those from the in-house synthesized ZnO nanofluid on all the substrates (D_0 = 1.42 - 1.62, and a = 0.04 - 0.06).

The BM cells from the in-house ZnO nanofluids on glass exhibited the smallest FD values (μ = 1.77) compared to the silicon substrates (h_2 and h_3 *vs.* h_1 in **Figure 6b**). This could be reconciled with the D *vs.* λ_{BM} trend, as the corresponding BM cell size was the smallest (M = 289 μm, **Figure 4**). In addition, the smallest FD value on glass may also be related to the lack of interpenetration between the smaller cells. ZnO nanopowder and ZnO powder nano/microfluids produced residual surface patterns (**Figure S8**) with the highest fiber density and the highest level of inter-cell penetration. Even though the BM cells varied widely in diameters λ_{BM}, from M = 101 μm for the ZnO powder patterns on glass (**Figure S10g**) to M = 558 μm for the ZnO nanopowder patterns on UVO-Si (**Figure S10f**), the fractal dimension

analysis revealed that all of them had average D values between $\mu \approx 1.82$ - 1.84 (**Figure 6c** and **e**) comparable to the BM cells produced from the in-house ZnO nanofluid on Si and UVO-Si (μ = 1.84 and 1.82, respectively), but much larger than the average fractal dimension for the BM cells on glass (μ = 1.77) (**Figure 6a**). This suggests that the smallest FD value on glass was also related to the lack of interpenetration/overlapping between BM cells.

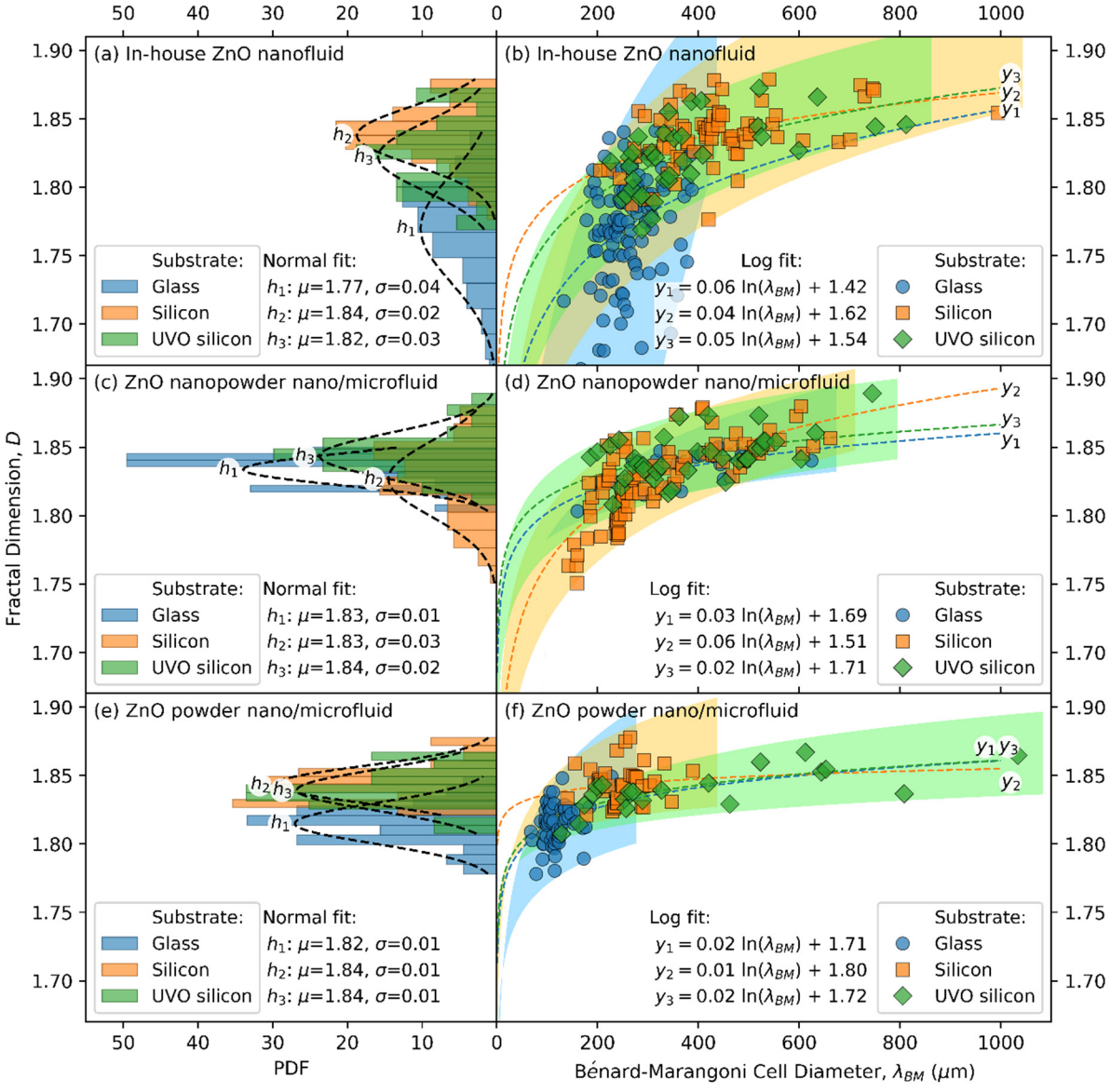

Figure 6. Box counting fractal dimension analysis of the solidified Bénard-Marangoni (BM) cells formed from drying ZnO nano/microfluids composed the in-house synthesized ZnO nanoparticles (**a- b**), ZnO nanopowder (**c-d**), and ZnO powder (**e- f**), on three different

substrates, microscope glass slide, Si, and UVO-Si. Left hand side plots (**a**, **c** and **e**) show fractal dimension (FD) distribution for all the samples, fitted with the normal (Gaussian) distribution function. Data fits are shown as dashed lines and labelled as h_1, h_2 and h_3, respectively for glass, Si and UVO-Si for each ZnO nano/microfluid. Parameters μ and σ stand for the mean D and its standard deviation. Right hand side plots (**b**, **d**, **f**) show the calculated box counting fractal dimension, D *vs*. the diameter of the investigated BM cell, λ_{BM}. Dashed lines labelled y_1, y_2, and y_3, show logarithmic fits. The scatter in the data is indicated by the colored regions that enclose the data points.

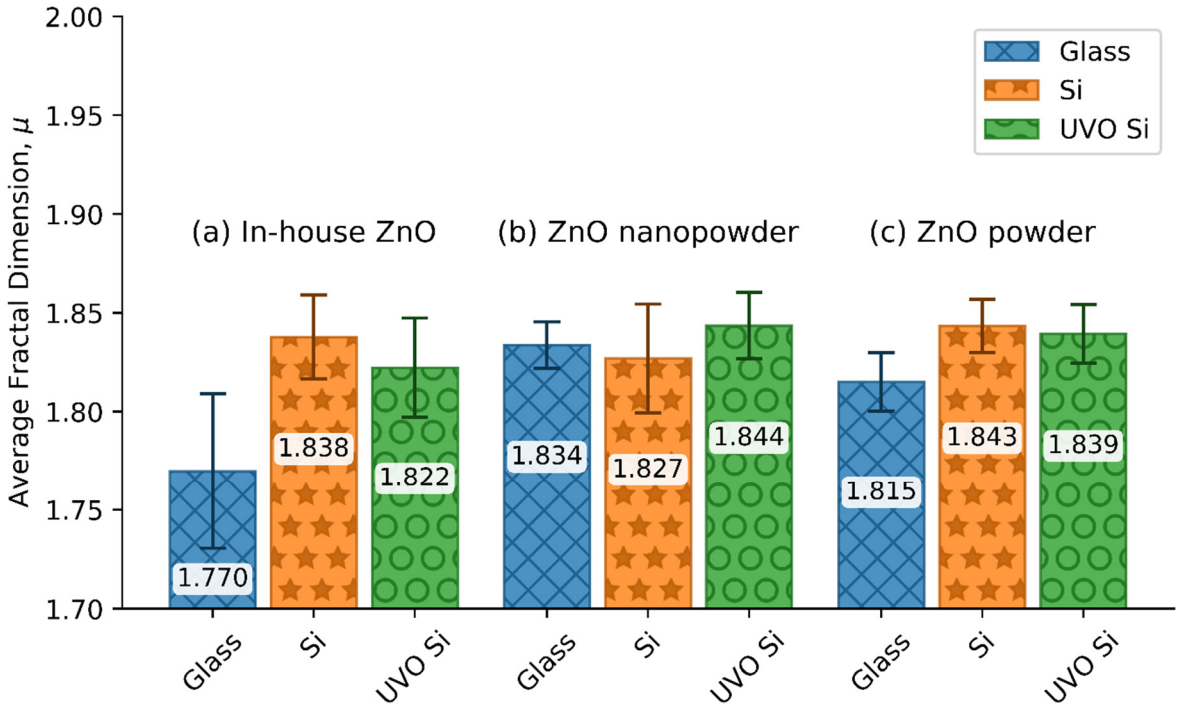

Figure 7. Average fractal dimension, μ, calculated for the Bénard-Marangoni (BM) cells produced from different nano/microfluids: (**a**) the in-house synthesized ZnO, (**b**) ZnO nanopowder, and (**c**) ZnO powder; formed on different substrates: glass (blue bars with "X" pattern), Si (orange bars with star "★" patterns), and UVO-Si (green bars with circle "O" patterns). The error bars are calculated as ± σ, which stand for standard deviation calculated from normal (Gaussian) distribution.

Further discussion on the effect of substrate surface chemistry

As shown in **Table 1**, all the substrates exhibited hydrophilic character, as their water contact angles CA were smaller than 90°. However, the hydrophilicity was in the decreasing of hydrophilized UVO-Si, microscope glass slide and untreated Si, evident both from the water CA and the polar components of the SFE γ^P.

The surface of a silicon wafer is covered with a native layer of silicon oxide or silica (SiO_2), which forms naturally when a silicon surface is exposed to air in ambient conditions (46). The surface of silicon oxide consists mainly of silanols (Si-OH), siloxanes (Si-O-Si), and their permutations (47). Silanol groups are responsible for hydrophilic interactions due to their ability to form the hydrogen bond with water. In contrast, siloxanes and other species present on the SiO_2 surface, such as Si-H, Si-CH_x and Si-F, are responsible for hydrophobic interactions due to their homopolar character (48). A prolonged UVO exposure of a silicon wafer in air leads to the formation of silanol groups in a reaction of chemical entities produced from bond breaking in the Si-O-Si surface structure and dissociation of water molecules (29). This in turn greatly increases the hydrophilicity of a UVO treated Si substrate.

The glass surface is composed of the same SiO_2 tetrahedral building block as crystalline silica. However, the arrangement of these tetrahedral units is characterized by the absence of long-range order and the presence of ring-like structures, caused by network modifier ions (Ca^{+2}, Mg^{2+}, Na^+, or K^+) and non-bridging oxygens (49). Nevertheless, it is expected that the surface chemistry of the microscope slides, made of silicate glasses, is governed by the relative populations of silanol (Si-OH), siloxide (Si-O^-), and siloxane (Si-O-Si) surface groups, similar to amorphous silica films (50).

Taking the above into account, the three substrates used in this work, microscope glass slide, silicon wafer and hydrophilized silicon wafer exhibited different levels of hydrophilicity due to different compositions of hydrophilic (silanols, siloxides) and hydrophobic (siloxanes)

groups present on their surfaces. The hydrophilized silicon wafer possessed the highest ratio of silanols, generated by the UVO exposure, followed by microscope glass slide, and unmodified silicon wafer.

In general, the solvent evaporation dynamics proximal to the surface and at the dewetting front is affected by the surface wettability by the dispersion, and in turn the substrate surface chemistry. Upon evaporation of a droplet of radius R with a contact angle θ on the substrate at the three-phase contact line, the evaporating flux $J(r)$ at a distance r from droplet center scales as $J(r) \propto (R - r)\lambda$, where $\lambda = (\pi - 2\theta)/(2\pi - 2\theta)$ (51). This indicates that the evaporation flux prominent in the coffee ring formation mechanism is similar on all the three substrates, due to the similar initial pinned CA values and those for the nano/microfluids. The significant difference among the three substrates is their hydrophilicity, as indicated by the different water CA values on these substrates and different SFE polar components γ^P, which would give rise to different affinities for water molecules and also the amphiphilic molecular clusters generated *in situ* upon evaporation (24).

In the mechanism described in (24), reactive ZnO particles are proposed to alter evaporation induced solvent *via in situ* generated molecular and particulate species. ZnO nanoparticles may undergo rapid chemical transformation into isobutylamine-ZnOH molecular complexes (iZMCs) of sub-nanometer in size, which further self-assemble into nanoclusters as stimulated by the presence of polar molecules – particularly trace amounts of water. The hydrolysis of isobutylamine by water encourages the formation of iZMCs. These surface active iZMCs and clusters accumulate at the sessile drop surface and the peripheral contact line, and would also adsorb to the substrate. As the drop thins, BM instabilities are triggered, and iZMC-cluster coalescence along multiple BM flows leads to the formation of the central cellular patterns. Concurrently, this dendritic cluster growth also occurs at the receding peripheral contact line on the substrate. Further drying drives iZMC organization on the substrate into crystal lattices

in the micro-dendrites in the final hierarchical polycrystalline surface structures. Here we show that different surface hydrophilicity of the substrate would affect its interactions with the iZMCs and their self-assembled clusters. This presumably would affect the cluster density, local viscosity, and solvent flows proximal to the substrate during evaporation. It would also influence the final recrystallization on the substrate in which the iZMCs reorganize into the crystal lattices, a process affected by the inter-cluster interactions and the cluster-substrate interactions, both of which would depend on the presence of trace amounts of water.

CONCLUDING REMARKS

We have observed that the solidified BM dendritic cells formed upon evaporation of sessile drops containing ZnO particulate dispersions in a mixed solvent on three different substrates varying in hydrophilicity. The BM cell size distribution and its fractal dimension both depended on the substrate on which evaporation occurred. The BM cells had the smallest diameters and density on the glass surface when compared to unmodified and hydrophilized silicon substrates for all the ZnO nano/microfluids studied. Meanwhile, the spoke-like radial BM cell structures formed on the UVO hydrophilized silicon had the largest diameters with the widest spread in dimensions.

Fractal dimensional analysis of the BM cells provided a quantitative description of the geometric properties of these structures, to describe their ruggedness or how much space it fills when the structure is scaled up or down (43-44). It was shown that the in-house ZnO nanofluid produced bigger BM cells with much higher degree of inter-cell overlapping on both unmodified and UVO treated silicon substrates ($D = 1.84 \pm 0.02$ and 1.82 ± 0.03, respectively) than on glass ($\mu \approx 1.77 \pm 0.04$). On the other hand, ZnO nano/microfluids prepared from the commercially acquired ZnO nanopowder and ZnO powder produced patterns of the highest coverage and level of overlapping of the BM cells, manifested in average D in range 1.82 - 1.84 on all the substrates. The observed trend of the fractal dimension D increasing with the

increasing BM diameter λ_{BM} is indicative of a two stage fractal growth, with the smaller BM cells representing growing fractals with a more open structure, and the larger mature BM dendrites possessing a more complicated structure with overlapping boundaries with adjacent BM cells.

As discussed in the previous work, the presence of water molecules is crucial for the moisture-assisted dissolution of ZnO nanocrystals dispersed in a mixture of cyclohexane and isobutylamine (25-26), as well as subsequent cluster formation and recrystallization on the substrate. We attribute the observed different BM cell characteristics (size distributions and FD values) to different surface chemistry of the substrates, particularly their hydrophilicity. Conversely, this provides a mechanism for controlling the morphology of hierarchical surface patterns created after the evaporation of a ZnO nano/microfluid sessile drop.

SUPPORTING INFORMATION

The Supporting Information (SI) associated with this article can be found, in the online version, at https://doi.org/XXX. The SI contains: SI.01: ZnO particles; SI.02: UV/Ozone treatment of Si wafer substrates; SI.03: Contact angle (CA) characterization and surface free energy (SFE) calculations; SI.04: Atomic force microscopy (AFM) of the substrates SI.05: Characterization of the residual surface patterns; SI.06: Bénard-Marangoni cell size distribution - log-normal fitting; and SI.07: Fractal dimension analysis of the Bénard-Marangoni cells.

ORC

Patryk Wąsik: 0000-0002-7447-7472

Annela M. Seddon: 0000-0002-5794-8500

Wuge H. Briscoe: 0000-0001-8025-960X

ACKNOWLEDGEMENTS

P.W. is supported by the UK Engineering and Physical Sciences Research Council (EPSRC) through the Bristol Centre for Functional Nanomaterials (BCFN) (grant no. 1371498). H.W. is supported by a Marie Skłodowska-Curie Individual Fellowship (Project Number 656830). W.H.B. would like to acknowledge funding from the EPSRC (EP/H034862/1 and Building Global Engagement in Research (BGER)), European Cooperation in Science and Technology (CMST COST) Action CM1101 "Colloidal Aspects of Nanoscience for Innovative Processes and Materials", and Marie Curie Initial Training Network (MCITN) on "Soft, Small, and Smart: Design, Assembly, and Dynamics of Novel Nanoparticles for Novel Industrial Applications" (NanoS3). Mr Jonathan Jones and Dr Sean Davis are thanked for their help with SEM imaging. Ms Anna Slastanova and Ms Lauren Matthews are acknowledged for their help with the contact angle measurements. Mx Kate Oliver is thanked for a discussion about the approach to the fractal dimension analysis of digital images. Ms Dajana Gubała is thanked for her help with AFM measurements.

REFERENCES

1. Maroto, J. A.; Pérez-Muñuzuri, V.; Romero-Cano, M. S., Introductory analysis of Bénard–Marangoni convection. *European Journal of Physics* **2007,** *28* (2), 311.

2. Bénard, H., Étude expérimentale des courants de convection dans une nappe liquide. — Régime permanent : tourbillons cellulaires. *J. Phys. Theor. Appl.* **1900,** *9* (1), 513-524.

3. Wesfreid, J. E., Scientific Biography of Henri Bénard (1874–1939). In *Dynamics of Spatio-Temporal Cellular Structures: Henri Bénard Centenary Review*, Mutabazi, I.; Wesfreid, J. E.; Guyon, E., Eds. Springer New York: New York, NY, 2006; pp 9-37.

4. Fauve, S., Henri Bénard and pattern-forming instabilities. *Comptes Rendus Physique* **2017,** *18* (9), 531-543.

5. Rayleigh, L., LIX. On convection currents in a horizontal layer of fluid, when the higher temperature is on the under side. *The London, Edinburgh, and Dublin Philosophical Magazine and Journal of Science* **1916,** *32* (192), 529-546.

6. Block, M. J., Surface Tension as the Cause of Bénard Cells and Surface Deformation in a Liquid Film. *Nature* **1956,** *178*, 650.

7. Pearson, J. R. A., On convection cells induced by surface tension. *J. Fluid Mech.* **1958,** *4* (5), 489-500.

8. Mutabazi, I.; Wesfreid, J. E.; Guyon, E., *Dynamics of Spatio-Temporal Cellular Structures: Henri Bénard Centenary Review*. Springer Tracts in Modern Physics: 2006; Vol. 207.

9. Getling, A. V.; Brausch, O., Cellular flow patterns and their evolutionary scenarios in three-dimensional Rayleigh-Bénard convection. *Phys. Rev. E* **2003,** *67* (4), 046313.

10. Han, W.; Lin, Z., Learning from "Coffee Rings": Ordered Structures Enabled by Controlled Evaporative Self-Assembly. *Angew. Chem. Int. Ed.* **2012,** *51* (7), 1534-1546.

11. Zhong, X.; Crivoi, A.; Duan, F., Sessile nanofluid droplet drying. *Adv. Colloid Interface Sci.* **2015,** *217*, 13-30.

12. Wang, H.; Wang, Z.; Huang, L.; Mitra, A.; Yan, Y., Surface Patterned Porous Films by Convection-Assisted Dynamic Self-Assembly of Zeolite Nanoparticles. *Langmuir* **2001,** *17* (9), 2572-2574.

13. Maillard, M.; Motte, L.; Ngo, A. T.; Pileni, M. P., Rings and Hexagons Made of Nanocrystals: A Marangoni Effect. *J. Phys. Chem. B* **2000,** *104* (50), 11871-11877.

14. Maillard, M.; Motte, L.; Pileni, M. P., Rings and Hexagons Made of Nanocrystals. *Adv. Mater.* **2001,** *13* (3), 200-204.

15. Nguyen, V. X.; Stebe, K. J., Patterning of Small Particles by a Surfactant-Enhanced Marangoni-Bénard Instability. *Phys. Rev. Lett.* **2002,** *88* (16), 164501.

16. Truskett, V. N.; Stebe, K. J., Influence of Surfactants on an Evaporating Drop: Fluorescence Images and Particle Deposition Patterns. *Langmuir* **2003,** *19* (20), 8271-8279.

17. Sakurai, S.; Furukawa, C.; Okutsu, A.; Miyoshi, A.; Nomura, S., Control of mesh pattern of surface corrugation via rate of solvent evaporation in solution casting of polymer film in the presence of convection. *Polymer* **2002,** *43* (11), 3359-3364.

18. Bassou, N.; Rharbi, Y., Role of Bénard−Marangoni Instabilities during Solvent Evaporation in Polymer Surface Corrugations. *Langmuir* **2009,** *25* (1), 624-632.

19. Bormashenko, E., Surface instabilities and patterning at liquid/vapor interfaces: Exemplifications of the "hairy ball theorem". *Colloids and Interface Science Communications* **2015,** *5* (Supplement C), 5-7.

20. Uchiyama, H.; Matsui, T.; Kozuka, H., Spontaneous Pattern Formation Induced by Bénard–Marangoni Convection for Sol–Gel-Derived Titania Dip-Coating Films: Effect of Co-solvents with a High Surface Tension and Low Volatility. *Langmuir* **2015,** *31* (45), 12497-12504.

21. Cai, Y.; Zhang Newby, B.-m., Marangoni Flow-Induced Self-Assembly of Hexagonal and Stripelike Nanoparticle Patterns. *J. Am. Chem. Soc.* **2008,** *130* (19), 6076-6077.

22. Suresh Singh, R.; Grimes, C. A.; Dickey, E. C., Fabrication of nanoporous TiO2 films through Benard-Marangoni convection. *Material Research Innovations* **2002,** *5* (3), 178-184.

23. Larouche, F.; Smiljanic, O.; Sun, X.; Stansfield, B. L., Solutal Bénard–Marangoni instability as a growth mechanism for single-walled carbon nanotubes. *Carbon* **2005,** *43* (5), 986-993.

24. Wu, H.; Briscoe, W. H., Morphogenesis of polycrystalline dendritic patterns from evaporation of a reactive nanofluid sessile drop. *Physical Review Materials* **2018,** *2* (4), 045601.

25. Wu, H.; Chen, L. X.; Zeng, X. Q.; Ren, T. H.; Briscoe, W. H., Self-assembly in an evaporating nanofluid droplet: rapid transformation of nanorods into 3D fibre network structures. *Soft Matter* **2014,** *10* (29), 5243-5248.

26. Wąsik, P.; Redeker, C.; Dane, T. G.; Seddon, A. M.; Wu, H.; Briscoe, W. H., Hierarchical Surface Patterns upon Evaporation of a ZnO Nanofluid Droplet: Effect of Particle Morphology. *Langmuir* **2018,** *34* (4), 1645-1654.

27. Wąsik, P.; Seddon, A. M.; Wu, H.; Briscoe, W. H., Dendritic surface patterns from Bénard-Marangoni instabilities upon evaporation of a reactive ZnO nanofluid droplet: A fractal dimension analysis. *J. Colloid Interface Sci.* **2019,** *536*, 493-498.

28. Sun, B.; Sirringhaus, H., Solution-Processed Zinc Oxide Field-Effect Transistors Based on Self-Assembly of Colloidal Nanorods. *Nano Lett.* **2005,** *5* (12), 2408-2413.

29. Lin, X.; Liao, G.; Tang, Z.; Shi, T., UV surface exposure for low temperature hydrophilic silicon direct bonding. *Microsyst. Technol.* **2009,** *15* (2), 317-321.

30. Vig, J. R., UV/ozone cleaning of surfaces. *J. Vac. Sci. Technol., A* **1985,** *3* (3), 1027-1034.

31. Owens, D. K.; Wendt, R. C., Estimation of the surface free energy of polymers. *J. Appl. Polym. Sci.* **1969,** *13* (8), 1741-1747.

32. Napolitano, A.; Ungania, S.; Cannata, V., Fractal Dimension Estimation Methods for Biomedical Images. In *MATLAB - A Fundamental Tool for Scientific Computing and Engineering Applications - Volume 3*, Katsikis, V. N., Ed. InTech: Rijeka, 2012; p Ch. 07.

33. Alligood, K. T.; Sauer, T. D.; Yorke, J. A., *Chaos: An Introduction to Dynamical Systems*. Springer New York: 2012.

34. Karperien, A. FracLac for ImageJ. http://rsb.info.nih.gov/ij/plugins/fraclac/FLHelp/Introduction.htm (accessed 4th Jun 2018).

35. Alam, A. U.; Howlader, M. M. R.; Deen, M. J., The effects of oxygen plasma and humidity on surface roughness, water contact angle and hardness of silicon, silicon dioxide and glass. *J. Micromech. Microeng.* **2014,** *24* (3), 035010.

36. Wang, H.; Yu, B.; Jiang, S.; Jiang, L.; Qian, L., UV/ozone-assisted tribochemistry-induced nanofabrication on Si(100) surfaces. *RSC Advances* **2017,** *7* (63), 39651-39656.

37. Dann, J. R., Forces involved in the adhesive process: I. Critical surface tensions of polymeric solids as determined with polar liquids. *J. Colloid Interface Sci.* **1970,** *32* (2), 302-320.

38. Ström, G.; Fredriksson, M.; Stenius, P., Contact angles, work of adhesion, and interfacial tensions at a dissolving Hydrocarbon surface. *J. Colloid Interface Sci.* **1987,** *119* (2), 352-361.

39. Żenkiewicz, M., Methods for the calculation of surface free energy of solids. *Journal of Achievements in Materials and Manufacturing Engineering* **2007,** *24* (1), 137-145.

40. Wlodek, M.; Kolasinska-Sojka, M.; Wasilewska, M.; Bikondoa, O.; Briscoe, W. H.; Warszynski, P., Interfacial and structural characteristics of polyelectrolyte multilayers used as cushions for supported lipid bilayers. *Soft Matter* **2017,** *13* (43), 7848-7855.

41. Smith, J. E.; Jordan, M. L., Mathematical and graphical interpretation of the log-normal law for particle size distribution analysis. *J. Colloid Sci.* **1964,** *19* (6), 549-559.

42. Zender, C. Particle size distributions: theory and application to aerosols, clouds, and soils. http://dust.ess.uci.edu/facts/psd/psd.pdf (accessed 12th Dec 2017).

43. Falconer, K. J., *Fractal geometry: mathematical foundations and applications*. Wiley: Chichester, 1990.

44. Rahman, M. S., Physical meaning and interpretation of fractal dimensions of fine particles measured by different methods. *J. Food Eng.* **1997,** *32* (4), 447-456.

45. Mandelbrot, B. B., *The Fractal Geometry of Nature*. Freeman and Company: New York, 1982.

46. Morita, M.; Ohmi, T.; Hasegawa, E.; Kawakami, M.; Ohwada, M., Growth of native oxide on a silicon surface. *J. Appl. Phys.* **1990,** *68* (3), 1272-1281.

47. Thomas, R. R.; Kaufman, F. B.; Kirleis, J. T.; Belsky, R. A., Wettability of Polished Silicon Oxide Surfaces. *J. Electrochem. Soc.* **1996,** *143* (2), 643-648.

48. Grundner, M.; Jacob, H., Investigations on hydrophilic and hydrophobic silicon (100) wafer surfaces by X-ray photoelectron and high-resolution electron energy loss-spectroscopy. *Appl. Phys. A* **1986,** *39* (2), 73-82.

49. Melcher, M.; Wiesinger, R.; Schreiner, M., Degradation of Glass Artifacts: Application of Modern Surface Analytical Techniques. *Acc. Chem. Res.* **2010,** *43* (6), 916-926.

50. Warring, S. L.; Beattie, D. A.; McQuillan, A. J., Surficial Siloxane-to-Silanol Interconversion during Room-Temperature Hydration/Dehydration of Amorphous Silica Films Observed by ATR-IR and TIR-Raman Spectroscopy. *Langmuir* **2016,** *32* (6), 1568-1576.

51. Jason, N. N.; Chaudhuri, R. G.; Paria, S., Self-assembly of colloidal sulfur particles influenced by sodium oxalate salt on glass surface from evaporating drops. *Soft Matter* **2012,** *8* (14), 3771-3780.

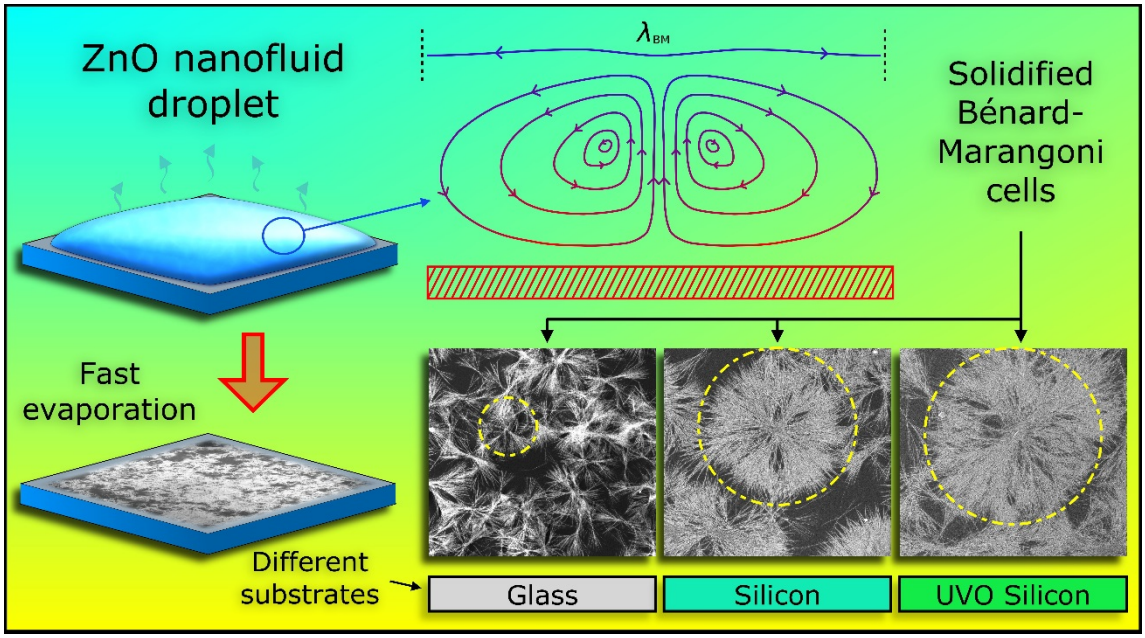

Table of Contents graphic